This is the Pre-Published Version.

This is the peer reviewed version of the following article: Zheng, B., Wu, Z., Guo, F., Ding, R., Mao, J., Xie, M., Lau, S. P., Hao, J., Large-Area Tellurium/Germanium Heterojunction Grown by Molecular Beam Epitaxy for High-Performance Self-Powered Photodetector. Adv. Optical Mater. 2021, 9, 2101052 , which has been published in final form at https://doi.org/10.1002/adom.202101052. This article may be used for non-commercial purposes in accordance with Wiley Terms and Conditions for Use of Self-Archived Versions. This article may not be enhanced, enriched or otherwise transformed into a derivative work, without express permission from Wiley or by statutory rights under applicable legislation. Copyright notices must not be removed, obscured or modified. The article must be linked to Wiley's version of record on Wiley Online Library and any embedding, framing or otherwise making available the article or pages thereof by third parties from platforms, services and websites other than Wiley Online Library must be prohibited.

Large-area Tellurium/Germanium Heterojunction Grown by Molecular Beam Epitaxy for High-performance Self-powered Photodetector

Beining Zheng, Zehan Wu, Feng Guo, Ran Ding, Jianfeng Mao, Maohai Xie, Shu Ping Lau, and Jianhua Hao**

Dr. B. Zheng, F. Guo, Dr. R. Ding, J. Mao, Department of Applied Physics, The Hong Kong Polytechnic University, Hung Hom, Hong Kong, P. R. China.
Z. Wu, Prof. S. P. Lau, Prof. J. Hao, Department of Applied Physics, The Hong Kong Polytechnic University, Hung Hom, Hong Kong, P. R. China. The Hong Kong Polytechnic University Shenzhen Research Institute, Shenzhen 518057, P. R. China.
E-mail: daniel.lau@polyu.edu.hk; jh.hao@polyu.edu.hk
Prof. M. Xie, Physics Department, The University of Hong Kong, Pokfulam Road, Hong Kong. P. R. China.

Keywords: (tellurium, semiconductor germanium, heterojunction, large-area growth, self-powered photodetectors)

As an attractive elemental semiconductor material, p-type tellurium (Te) with a narrow bandgap provides high carrier mobility, strong light-matter interactions in a wide spectral range, and good chemical stability, which enlightens the potential in optoelectronic devices. However, the applications are impeded by weak carrier separation and vague potential in scaling-up. In this work, the integration of Te and conventional semiconductor germanium (Ge) is designed. Through molecular beam epitaxy (MBE) method, large-area and uniform Te films with high crystallinity are directly deposited on the Ge substrates. The difference in work function between Te and Ge layer leads to a built-in electric field which can enhance carrier separation effectively. As a result, a self-powered splendid photovoltaic performance is observed in the MBE grown Te/Ge vertical heterojunction with current on/off ratio over 10^3, responsivity (R) 523 $mA \cdot W^{-1}$, and specific detectivity (D*) 9.50×10^{10} $cm \cdot Hz^{1/2} \cdot W^{-1}$ when illuminated by near-infrared light (980 nm, 2.15 $\mu W \cdot cm^{-2}$). Furthermore,

excellent stability and high response speed of the ultrathin heterostructure offer significant application value for multipurpose photoelectric device.

Introduction

Monoelemental tellurium (Te), a narrow-band gap semiconductor, has aroused tremendous attention in high-efficiency photoconductor application due to its intriguing property advantages.[1-3] The strong intrinsic hole mobility of Te, which is up to hundreds to thousands of $cm^2 \cdot V^{-1} \cdot s^{-1}$ at room temperature and much higher than that of mostly studied 2D MoS_2, makes Te enormously promising for fabricating ultrathin photodetectors with high sensitivity and fast response speed.[2, 4-7] Tunable bandgap of Te (0.3-1 eV) suggests a broadband spectral response covering the broad spectral range spanning from ultraviolet to mid-infrared region.[8] Furthermore, its intrinsic covalent bonding form with a long chiral-chain structure also grants ambient stability and innovative flexibility for the promising candidates of multi-function devices.[2, 9, 10] In addition, the manifold of superior photoresponse performances of Te like high gating modulation, thickness dependence, piezoelectricity tunability, and polarization sensitivity were also reported in its prepared nanostructure. [10-13] However, due to the helical chain structural configuration, large-area preparation of Te materials with desired crystalline phase or thickness is limited by sensitivity to experimental conditions and vague potential in scaling-up. More than that, indirect band gap and long intrachain carrier diffusion distance cannot allow efficient separation of photoexcited electron-hole pairs in pristine Te-based photodetectors, which constantly suffer from low detectivity (~ 2.4×10^6 Jones, Jones = $cm \cdot Hz^{1/2} \cdot W^{-1}$) and poor current on/off ratio

(I_{on}/I_{off} ratio). [3, 14] These key elements are stonewalling the Te optoelectronic widespread endeavor.

Generally, single-crystal substrates with high activity surfaces have proved to be effective in ensuring uniform film growth due to their strong interfacial binding strength.[15] Simultaneously, utilizing integrated junction features, layered materials (such as graphene, MoS_2, WSe_2, GeSe, $GaTe_2$ and black phosphorus), perovskite, and other oxide semiconductor compounds have made use of their respective advantages to conduct many extraordinary properties for photodetector applications.[16-23] Hence constructing integrated junctions is a rational scenario for catalytic growth of the large area and high crystalline-quality Te layers over substrate surfaces. If initial multiple nucleations of the Te seeds is induced by the high activity of the substrate surface, high-density seeds can grow and coalesce into a uniform layer. Meanwhile, it is deemed that the constructed interfaces, especially with optimizing band energy alignment properties, can facilitate efficient electron-hole pair separation. [24, 25] Unfortunately, although a variety of bottom-up synthesis techniques and routes (e.g., hydrothermal synthesis, vapor phase deposition, pulsed laser deposition) have been employed, the difficulty in deriving large-scale, high-quality Te crystalline form, in particular for integrated structure implementation, still undermines the exploration of its optoelectronic properties.[11, 26, 27] Until now, via integrating similar anisotropic and isomorphous characteristics materials, only few Te-based heterostructures like roll-to-roll Te@Se nanotube and analogous heterostructure (Te@Bi, and Te/Bi_2Se_3@Se core/shell) concerned over optoelectronic property were fabricated by chemical

transformation templating technique. Their photoresponsivity and photocurrent density were found to be significantly enhanced. [28-30] Considering poor control in thickness uniformity, small size of the derived materials, solution synthetic processing route and aqueous working environments, it remains pressing to alter the fact of the absence of Te integrated junctions.

For constructing high-speed and broad-spectrum optoelectronic devices, conventional semiconductor germanium (Ge) with larger carrier mobility and smaller band gap than Si is one of the ideal paradigms, especially in regard to its excellent band engineering advantage and low cost, mature and compatible processing technology. [31] Furthermore, Ge with high surface catalytic activity is conducive to induce the formation of more compact Te seeds, which would tend to spawn a desirable merged morphology. Based on the foregoing considerations, the integration of a hybrid Te and Ge heterojunctions is a feasible and more accessible scenario to construct innovative optoelectronic devices. Herein, large-area Te/Ge vertical heterojunctions are successfully fabricated through direct growth of Te continuous layer on the Ge wafer using molecular beam epitaxy (MBE) technique. Significantly, the Te/Ge heterojunctions exhibit pronounced photovoltaic activity. Moreover, the photodetector exhibits high performance with detectivity of 9.50×10^{10} cm·Hz$^{1/2}$·W^{-1} and I_{on}/I_{off} ratio over 10^3 (under 980 nm, 2.15 μW·cm^{-2} near-infrared light illumination). The Te/Ge photodetector shows excellent characteristics in terms of wide photoresponse range of visible-near infrared, ultrafast response speed and robust environmental stability. These key parameters are comparable and even higher than previously reported Te-based

photodetectors (Table S1, Supporting Information). The generality of this work suggests that Te-based junction optoelectronic devices have potential application in future optoelectronic devices.

Results and Discussion

The crystalline nature of as-grown Te thin films was studied through X-ray diffraction (XRD) measurements, as shown in **Figure 1**(a), from which the typical XRD patterns corresponding to (100), (101), and (200) diffraction peaks of Te hexagonal structure can be recognized. These diffraction peaks can be perfectly indexed to the JCPDF card number: 36-1452 for tellurium, and the strong diffraction of the (h00) planes indicates highly preferred $[10\bar{1}0]$ orientation of the growth. **Figure 1**(b) exhibits the Raman spectrum of an as-grown Te thin film, where three Raman-active modes can be observed. The most intense Raman peak located at ~ 122 cm^{-1} is related to the A_1 mode, corresponding to the chain-expansion vibration of Te atoms along the basal plane. Additionally, Raman peaks related to degenerate E_1 mode (94 cm^{-1}) and E_2 mode (142 cm^{-1}) can also be identified, which are caused by the asymmetric bond-stretching along *c*-axis and assigned to predominately bond-bending and bond-stretching types, respectively. The observed characteristic Raman vibration modes of high-crystalline trigonal tellurium are in agreement with previous reports. [32] The micro-crystalline nature of as-grown Te films was further studied through a high-resolution transmission electron microscope (TEM). As shown in **Figure 1**(c), the continuous lattice of the Te crystal with characteristic lattice fringe spacing of 3.25 Å can be observed clearly, which is assignable to the (100) lattice spacing of quasi-2D chiral-chain tellurene. To

provide further insight into the large-area crystallization homogeneity of Te film and the controllable construction of Te/Ge heterostructure, electron backscatter diffraction (EBSD) mapping was carried out in millimeter scale, as shown in **Figure 1**(d). According to the differential color matching of inverse pore figure (IPF), a highly $[10\bar{1}0]$-oriented Te crystalline film grown uniformly in a large area is evidenced, which are consistent with XRD results. The tests for another area of samples and Ge substrate are presented in **Figure S2** (Supporting Information).

To analyze the chemical states of Te/Ge interface, X-ray photoelectron spectroscopy (XPS) measurements were performed by repeating the etching process to the prepared heterojunction. Depth profiling XPS spectra for 5 different etching levels are shown in **Figure 1**(e). Depth range from the position Ge signal which was just detected to the bare Ge substrate is defined so as to intuitively examine the interface structure. The peaks located at 572.98 and 583.38 eV are assigned to Te $3d_{5/2}$ and Te $3d_{3/2}$ doublets, respectively. The peak at 29.48 eV corresponds to Ge 3d. The initial pronounced Ge 3d peak at 29.48 eV emerges after 18 s of etching, indicating the absence of Ge in the top layers of the original unetched sample, and the consistent peak corresponding to the Te 3d that nearly vanishes after 84 s etching, indicating that the Te is fully eroded at that time. During the etching process, the intensity decrease in Te 3d peaks is identified, instead, variation of Ge 3d peak intensity behaves in the opposite way. Remarkably, no obvious shift of the Te $3d_{3/2}$, Te $3d_{5/2}$ and Ge 3d signals is detected, which confirms that the formation of Ge-Te bond is not dominant on the heterostructure interface. [33, 34] The accurate comparison of spectra between Te film surface without

etching and the interface mixing state with 36 s etching level is shown in **Figure 1**(f), which further points to no shift of the Te characteristic peaks between that near the interface of Te/Ge and pure Te. The barely visible XPS peak of Te oxide indicates the Te film possesses excellent air stability, which has shown quite a difference to previous work. [35]

From the SEM and AFM characterization, the morphology results of the Te film presents uniform and compact stacked structure with regular orientations, as shown in **Figure 2**(a) and (b). Complete substrate coverage guarantees the stable performance of the Te/Ge photodetector device. The thickness of the Te film was obtained by AFM measurement cross the edge of Te film, as shown in **Figure 2**(c). The resultant height profile shown in **Figure 2**(d) exhibits a thickness approximately 18 nm. According to the above investigations, one can conclude that highly crystalline Te film was homogenously grown on a large-scale single crystal Ge substrate, and a representative Te/Ge vertical heterostructure is successfully constructed for further development of optoelectronic applications.

To explore the optoelectronic performance of the large-size Te film integrated with Ge, a simple photodetector had been fabricated. The sequential fabrication process and schematic diagram of the Te/Ge heterojunction photodetector are illustrated in **Figure S3** (Supporting Information). The *I-V* curves of Te/Ge heterojunction photodetector under dark condition in linear and logarithmic coordinates scale under dark condition are presented in **Figure 3**(a). Notably, the rectifying behavior of the device shows the large reverse current ($I_{reverse}$) is stronger than that of the forward current ($I_{forward}$),

indicating that a backward diode is formed. The photodiode shows the reverse rectification ratio of 2.2 at ± 1 V. The ideality factor (n) is a dimensionless parameter which can be calculated through the obtained slope of the linear section of the semi-In I-V curves. It can be deduced from the following equation：

$$R = \frac{I_{ph}}{k_B T} \frac{dV}{d \ln I} \qquad \textbf{(Equation 1)}$$

where q, kB, and T are unit charge, Boltzmann's constant, and Kelvin temperature, respectively. For the Te/Ge heterojunction, the values of ideality factor for dark condition I-V measurements can be calculated to be 1.66. The small ideality factor confirms the quality of the Te/Ge heterojunction. And there is a deviance from the perfect value (n = 1). This deviance is mainly caused by the presence of fabrication induced defects, distribution of barrier heights and inhomogenities on the Te/Ge heterojunction interface.

The *I-V* curves of the device under several typical visible light irradiation are shown in **Figure 3**(b). The current at reverse bias direction increases obviously, and the apparent photovoltaic behaviors under light illumination indicate Te/Ge heterojunction suitable to serve as a self-powered photodetector. In view of the linear current and voltage relationship between Te film and graphene layer electrode, this turns out to be ohmic contact formed at the interface (**Figure S6**, Supporting Information). **Figure 3**(c) depicts the transient response results for the visible wavelength lights. The Te/Ge heterojunction photodetector was operated for a consecutive response measurement. The switch results after 2000 cycles are depicted in **Figure 3**(d). The consecutive response with no degradation illustrates excellent durability and reproducibility of the

proposed photodetector.

The working principle of the Te/Ge heterojunction photodetector can be made clear by p-n junction-based photovoltaic mechanism. The interfacial charge effect is crucial for the migration of carriers and was analyzed by Scanning Kelvin probe microscopy (KPFM). Based on the line profile across the heterojunction region, the surface potential mapping between Te and Ge is shown in **Figure 3**(e). It is observed that the surface potential increases from left (n-Ge) to right (p-Te) and has a noticeable rise at the interface. This means that p-Te has a higher Fermi energy level (~ 0.12 V) than that of n-Ge and provides direct evidence of the existence of built-in electric field inside the Te/Ge heterojunction. The typical bandgap data of Te and Ge is referred to determine their respective relative positions between conduction band minimum (E_C) and valence band maximum (E_V).[36, 37] According to the above information, the energy band structure diagrams of p-type Te and n-type Ge are concluded, where E_F of Te and Ge are close to their E_V and E_C, respectively. **Figure 3**(f) depicts the band energy level diagram of the heterojunction. The built-in electric field between Ge and Te heads to dissociation of the photoinduced charge pairs which diffuse to the depletion interface.[38] On the other hand, p-type Te is also a superior channel material because of its high carrier mobility. Therefore, by combining with Te fast carrier transport, the internal electric field effect in Te/Ge heterogeneous structure delivers significant enhancement in the photodetection performance compared to the conventional Te photoconductance.

To further investigate the photoresponse of the Te/Ge heterojunction photodetector, 980 nm laser as the near infrared range light (NIR) source was selected

to carry out the performance test with varied illumination intensity. **Figure 4**(a) shows the *I-V* curves measured under a series of light intensity and dark conditions. Apparently, the device exhibits a pronounced photocurrent under NIR light (980 nm), as well as monochromatic blue light (465 nm) (**Figure S8**, Supporting Information), and the reverse current highly depends on the light intensity. A large short-circuit current (I_{sc}) of 1.89 μA and an open-circuit voltage (V_{oc}) of 0.15 V can be achieved for 980 nm light under a light intensity of 4.03 $mW \cdot cm^{-2}$, as shown in **Figure 4**(b). Photoresponse characteristic, as displayed in **Figure 4**(c), demonstrates that I_{on}/I_{off} ratio of the photodetector is highly dependent on light intensity at zero bias. The device can follow the on-off pulsed irradiation with sharp photocurrent rise and fall edges, yielding the highest I_{on}/I_{off} ratio value of 1.4×10^3 under a light intensity of 4.04 $mW \cdot cm^{-2}$. A quantitative relationship is derived between the photocurrent versus incident light intensities at zero external bias voltage, which exhibits a good power-law dependence, $I_{Ph} \sim P_{\theta}$, and is plotted in **Figure 4**(d). The exponent θ of 0.48 for 980 nm light is noninteger and smaller than that of low trap state junctions (θ ≈ 1), which can be associated with the trap states on the Te and Ge wafer interface. [39, 40] As the key figure-of-merit parameters to evaluate the performance of a photodetector, responsivity (*R*) and detectivity (*D**) of a photodetector represent the efficiency of the photodetector responds to the exciting signals and the ability of the photodetector to detect weak exciting signals from process noise, respectively. The modulation relationship of responsivity (*R*) and detectivity (*D**) to the exciting intensity is plotted in **Figure 4**(e). The equations and the noise level per unit bandwidth (1 Hz) are included in Supporting

Information (Equations S1, S2, S3 and S4, **Figure S10**). Among all noise sources, the dark current dominated by short noise only is considered that for calculating detectivity. [41, 42] And the best responsivity (*R*) and detectivity (*D**) value are calculated to be 523 $mA \cdot W^{-1}$ and 9.50×10^{10} $cm \cdot Hz^{1/2} \cdot W^{-1}$ (Jones) (980 nm, 2.15 $\mu W \cdot cm^{-2}$) in the self-power mode, respectively. Correspondingly, external quantum efficiency (*EQE*) of this photodetector is plotted in **Figure 4**(f). The detectivity value is superior to other Te-based photodetectors (10^6-10^9 Jones), and the orders of magnitude improvement can be partly attributed to the lower dark current in a self-powered mode. [3] The decrease of all the above metrics with exciting light intensity increasing is probably due to the self-heating at a high light intensity, enhancing recombination possibility of charge carriers. [43] The variation tendencies were further validated by the 465 nm radiation (**Figure S8**, Supporting Information).

Photodetectors are much desirable to adapt to the growing demands with the surge of Internet of things, artificial intelligence, and other emerging fields, for which high stability in ambient condition and high response speed of the detectors is crucial. The photoresponse performance of the as-fabricated Te/Ge photodetector was maintained even after being stored in air for one month without any protection, as shown in **Figure 5**(a). The detailed measurements about long-term stability are presented in **Figure S10** (Supporting Information). The results exhibit excellent device stability and can be ascribed to the superior stable characteristic of Te in air. [2, 11] Furthermore, to evaluate the response speed of the Te/Ge heterostructure device, the responses to different frequency signals were investigated by monitoring the variation of photovoltage using

an oscilloscope. **Figure 5**(b) shows representative temporal responses to 980 nm pulsed laser signals with frequencies of 1, 2, and 5 kHz, respectively. The time-dependent normalized photocurrent to pulsed light signals with different visible radiation wavelengths is illustrated in **Figure S11** (Supporting Information). Although a pronounced degradation under 5 kHz frequency is observed, the Te/Ge heterostructure photodetector exhibits a fast, stable, and reversible photoresponse performance under these different frequency light signals. To fully exploit the potential of the Te/Ge heterostructure photodetector for higher frequency detection, the relative balance defined as $[(I_{max}-I_{min})/I_{max}]$ was measured with the wide frequency range of 1 Hz-100 kHz. From the relation between $[(I_{max}-I_{min})/I_{max}]$ and frequency as shown in **Figure 5**(c), a wide frequency response range over 100 kHz for the Te/Ge heterostructure is achieved. The relative balance decayed by about 25% at 5 kHz and therefore the 3 dB frequency ($f_{3\ dB}$) which is defined as the cutoff frequency is deduced to be ~5 kHz. [44]

In addition, as key figures to identify the speed of a photodetector, the rise time (t_{rise}) and decay time (t_{decay}) for the Te/Ge heterostructure can be extracted from the enlarged rise and fall edges of response curves, as shown in **Figure 5**(d). Based on the definition (the time interval rising from 10% to 90% of the peak value or vice versa), a small rise time (t_{rise}) and decay time (t_{decay}) at 1 kHz can be estimated as 26 and 60 μs, respectively. The fabricated photodetector has the fastest response, much faster than the existing Te-based counterparts. These results unambiguously elaborate that Te/Ge heterojunction photodetector is well suited for high-speed photoelectric applications. For the general view about response time of a photodiode-type photodetector, the

response time is mainly determined by the transit time of the carriers, which is inversely proportional to the carrier mobility and applied bias, but proportional to the film thickness. Therefore, the reasons of the limited response times can be summarized as follows: (1) the strong intrinsic hole mobility of Te material; (2) due to the existence of built-in electric field, no external bias was applied during the operation of the device; (3) the small thickness of the Te film and electrode layer. It should be noted that: for the Te/Ge heterostructure, the response time is indeed dominated by the self-limited depletion region. The photoresponse time is mainly determined by the lifetime of the electronic trap states on the heterojunction interface. The existence of interface defects traps the carrier drift and reduces the corresponding speed. With device optimizing in the future, the photoresponse time metrics can get further promotion in Te-based optoelectronic devices.

Conclusion

In summary, the Te/Ge heterojunction was successfully fabricated by depositing Te film on an n-type Ge substrate using the MBE method. Surface bonding configurations of substrate alter the Te chain growth mode along with low-energy well-defined facets and induce the formation of large-area high crystalline-quality Te film with compact structure. To place our findings in a broader context, we conclude that the relatively versatile growth strategy and the wide range of three-dimension materials surfaces make it possible to realize the reliable fabrication of Te crystal. Furthermore, the virtue of interfacial built-in electric field on the vertical heterostructure interface is beneficial to facilitating the separation of photo-generated carriers. The heterojunction

photodetector is endowed with the self-powered nature and exhibits a multiband spectrum response ranging from visible to NIR light with a high responsivity of 523 $mA \cdot W^{-1}$, and specific detectivity of 9.50×10^{10} $cm \cdot Hz^{1/2} \cdot W^{-1}$, I_{on}/I_{off} ratio over 10^3 (under 980 nm, 2.15 $\mu W \cdot cm^{-2}$ near-infrared light illumination), which represents the best results achieved for Te-based photodetectors so far. In addition, excellent advantages of high stability and high response speed provide a potential for multi-purposes. Although optimizing device's processing is needed in the future study, our detector achieves the first direct wafer-scale combination of Te and mature semiconductor material and will inject new impetus to the development of Te-based optoelectronic applications.

Experimental Section

Film Deposition

Te deposition was carried out in a FERMI MBE system with a base pressure of ≈1×10^{-10} Torr and a background pressure of ≈ 3×10^{-10} Torr during growth. The flux of Te was generated using a standard Knudsen cell with operation temperature at 315 °C. Before loading into the load lock, the substrates Ge wafers（Sb-doped n-type, 1-10 $\Omega \cdot cm^{-1}$ resistivity） were ultrasonicated in acetone and isopropanol for 10 min, respectively. Prior to Te growth, the substrates were degassed at 500 °C for 30 min, and then cooled to the growth temperature. The thermocouple indicated growth temperature was 100°C and its variation was within 0.2 °C throughout the entire deposition process. To improve the film crystallinity, the as-prepared samples were slowly cooled down to room temperature at 1 °C per minute. The variation of vacuum degree is that: the chamber pressures during the growth is 3×10^{-10} Torr, and that after the growth process

is approximate 9×10^{-10} Torr.

Material Characterization

The crystallinity and chemical compositions of the fabricated heterojunctions were characterized by using XRD (Rigaku smart lab) with Cu Kα radiation (λ = 1.5406 Å) and confocal Raman spectroscopy (Witec alpha 300 R). Microstructure of the heterojunction was studied by high-resolution TEM (JEOL Model JEM-2010). Morphological images of the heterojunction were obtained by using SEM (Tescan VEGA3) and AFM (Asylum Research MFP-3D). Interfacial structures and surface potential of the Te/Ge heterojunction were probed by SKPM (Asylum Research MFP-3D) mode. The microstructural analysis was performed via field emission gun scanning electron microscopy (FEG-SEM, LEO 1530) equipped with EBSD system (Oxford Instruments NordlysNano EBSD Detector with AZtecHKL), with fine adjustment on tilt-angle of ~ 70°, where the electron-voltage was controlled at 20 kV. XPS was obtained from the Thermo Scientific Nexsa X-Ray Photoelectron Spectrometer System equipped with a Monochromatic and focused 12 kV Aluminum Kα X-ray source.

Device Fabrication

To construct Te/Ge heterojunction test device, glassy graphene (multilayer graphene on copper foil) was directly formed through a typical wetting-transferred method and then coated on the top of Te layer as the transparent top electrode. Afterwards, the graphene and Ge substrate were wire-bonded with silver leads using silver paste (RS Components 186-3600).

Optoelectronic Measurements

Optoelectronic characterization of the heterojunction device was performed on a

semiconductor parameter analyzer system (Keithley 2410). The light sources included in the measurements are: commercial LEDs with different fixed wavelengths used to produce the monochromatic visible light and a 980 nm laser module used to offer a near infrared range light. The laser spot size is 3.8 cm^2, and the spot size of visible LED is 4.5 cm^2. These spot areas are small enough compared to the device size. Therefore, the illumination can be ensured to focus on the channel part. There is not any substrate part irradiated. To evaluate the photoresponse speed of the heterojunctions, pulsed optical signals with varying frequencies were produced by driving light sources with a function generator (KEITHLEY 3390 arbitrary waveform generator), and then the output photocurrent was recorded with a digital oscilloscope (LeCroy WaveSurfer 62Xs).

Supporting Information

Supporting Information is available from the Wiley Online Library or from the author.

Acknowledgements

B. Zheng and Z. Wu have equal contributions to this work. This work was supported by the grants from the National Natural Science Foundation of China (No. 51972279), Science, Technology and Innovation Commission of Shenzhen (Project no. JCYJ 20180507183424383), Research Grants Council of Hong Kong (GRF no. PolyU 153023/18P and CRF no. C7036-17W) and PolyU Grant (1-ZVGH).

Received: ((will be filled in by the editorial staff))
Revised: ((will be filled in by the editorial staff))
Published online: ((will be filled in by the editorial staff))

References:

[1] W. Wu, G. Qiu, Y. Wang, R. Wang, P. Ye, *Chem. Soc. Rev.* **2018,** *47,* 7203.

[2] Y. Wang, G. Qiu, R. Wang, S. Huang, Q. Wang, Y. Liu, Y. Du, W. A. Goddard, M. J. Kim, X. Xu, P. D. Ye, W. Wu, *Nat. Electron.* **2018,** *1,* 228.

[3] Z. Xie, C. Xing, W. Huang, T. Fan, Z. Li, J. Zhao, Y. Xiang, Z. Guo, J. Li, Z. Yang,

B. Dong, J. Qu, D. Fan, H. Zhang, *Adv. Funct. Mater.* **2018,** *28,* 1705833.

[4] G. Zhou, R. Addou, Q. Wang, S. Honari, C. R. Cormier, L. Cheng, R. Yue, C. M. Smyth, A. Laturia, J. Kim, W. G. Vandenberghe, M. J. Kim, R. M. Wallace, C. L. Hinkle, *Adv. Mater.* **2018,** *30*, 1803109.

[5] C. Zhao, C. Tan, D. H. Lien, X. Song, M. Amani, M. Hettick, H. Y. Y. Nyein, Z. Yuan, L. Li, M. C. Scott, A. Javey, *Nat. Nanotechnol.* **2020,** *15,* 53.

[6] Z. Yu, Z.-Y. Ong, S. Li, J.-B. Xu, G. Zhang, Y.-W. Zhang, Y. Shi, X. Wang, *Adv. Funct. Mater.* **2017,** *27,* 1604093.

[7] J. A. del Alamo, *Nature* **2011,** *479,* 317.

[8] C. Shen, Y. Liu, J. Wu, C. Xu, D. Cui, Z. Li, Q. Liu, Y. Li, Y. Wang, X. Cao, H. Kumazoe, F. Shimojo, A. Krishnamoorthy, R. K. Kalia, A. Nakano, P. D. Vashishta, M. R. Amer, A. N. Abbas, H. Wang, W. Wu, C. Zhou, *ACS Nano* **2020,** *14,* 303.

[9] Y. Liu, W. Wu, W. A. Goddard III, *J. Am. Chem. Soc.* **2018,** *140,* 550.

[10] L. Tong, X. Huang, P. Wang, L. Ye, M. Peng, L. An, Q. Sun, Y. Zhang, G. Yang, Z. Li, F. Zhong, F. Wang, Y. Wang, M. Motlag, W. Wu, G. J. Cheng, W. Hu, *Nat. Commun.* **2020,** *11,* 2308.

[11] M. Amani, C. Tan, G. Zhang, C. Zhao, J. Bullock, X. Song, H. Kim, V. R. Shrestha, Y. Gao, K. B. Crozier, M. Scott, A. Javey, *ACS Nano* **2018,** *12,* 7253.

[12] J. Peng, Y. Pan, Z. Yu, J. Wu, J. Wu, Y. Zhou, Y. Guo, X. Wu, C. Wu, Y. Xie, *Angew. Chem., Int. Ed. Engl.* **2018,** *57,* 13533.

[13] S. Dang, S. D. Kang, T. Dai, X. Y. Ma, H. W. Li, W. Q. Zhou, G. L. Wang, P. Hu, Y. Sun, Z. H. He, F. M. Yu, X. Zhou, S. X. Wu, S. W. Li, *Nanotechnology* **2020,** *31,* 095502.

[14] Z. Shi, R. Cao, K. Khan, A. K. Tareen, X. Liu, W. Liang, Y. Zhang, C. Ma, Z. Guo, X. Luo, H. Zhang, *Nano-Micro Lett.* **2020,** *12,* 99.

[15] J. H. Lee, E. K. Lee, W. J. Joo, Y. Jang, B. S. Kim, J. Y. Lim, S. H. Choi, S. J. Ahn, J. R. Ahn, M. H. Park, C. W. Yang, B. L. Choi, S. W. Hwang, D. Whang, *Science* **2014,** *344,* 286.

[16] X. Li, M. Zhu, M. Du, Z. Lv, L. Zhang, Y. Li, Y. Yang, T. Yang, X. Li, K. Wang, H. Zhu, Y. Fang, *Small* **2016,** *12,* 595.

[17] L. Wang, J. Jie, Z. Shao, Q. Zhang, X. Zhang, Y. Wang, Z. Sun, S.-T. Lee, *Adv. Funct. Mater.* **2015,** *25,* 2910.

[18] E. Wu, D. Wu, C. Jia, Y. Wang, H. Yuan, L. Zeng, T. Xu, Z. Shi, Y. Tian, X. Li, *ACS Photonics* **2019,** *6,* 565.

[19] S. H. A. Jaffery, J. Kim, G. Dastgeer, M. Hussain, A. Ali, S. Hussain, J. Eom, S. Hong, J. Jung, *Adv. Mater. Interfaces* **2020,** *7,* 2000893.

[20] S. Yang, C. Wang, C. Ataca, Y. Li, H. Chen, H. Cai, A. Suslu, J. C. Grossman, C. Jiang, Q. Liu, S. Tongay, *ACS Appl. Mater. Interfaces* **2016,** *8,* 2533.

[21] X. Ren, Z. Li, Z. Huang, D. Sang, H. Qiao, X. Qi, J. Li, J. Zhong, H. Zhang, *Adv. Funct. Mater.* **2017,** *27,* 1606834.

[22] F. Cao, L. Meng, M. Wang, W. Tian, L. Li, *Adv. Mater.* **2019,** *31,* 1806725.

[23] C. Zhao, Z. Liang, M. Su, P. Liu, W. Mai, W. Xie, *ACS Appl. Mater. Interfaces* **2015,** *7,* 25981.

[24] T. Mueller, F. Xia, P. Avouris, *Nat. Photonics* **2010,** *4,* 297.

[25] H. Yuan, X. Liu, F. Afshinmanesh, W. Li, G. Xu, J. Sun, B. Lian, A. G. Curto, G. Ye, Y. Hikita, Z. Shen, S. C. Zhang, X. Chen, M. Brongersma, H. Y. Hwang, Y. Cui, *Nat. Nanotechnol.* **2015,** *10,* 707.

[26] Q. Wang, M. Safdar, K. Xu, M. Mirza, Z. Wang, J. He, *ACS Nano* **2014,** *8,* 7497.

[27] A. Apte, E. Bianco, A. Krishnamoorthy, S. Yazdi, R. Rao, N. Glavin, H. Kumazoe, V. Varshney, A. Roy, F. Shimojo, E. Ringe, R. K. Kalia, A. Nakano, C. S. Tiwary, P.

Vashishta, V. Kochat, P. M. Ajayan, *2D Mater.* **2018,** *6,* 015013.

[28] W. Huang, Y. Zhang, Q. You, P. Huang, Y. Wang, Z. N. Huang, Y. Ge, L. Wu, Z. Dong, X. Dai, Y. Xiang, J. Li, X. Zhang, H. Zhang, *Small* **2019,** *15,* 1900902.

[29] Y. Zhang, F. Zhang, L. Wu, Y. Zhang, W. Huang, Y. Tang, L. Hu, P. Huang, X. Zhang, H. Zhang, *Small* **2019,** *15,* 1903233.

[30] Y. Zhang, F. Zhang, Y. Xu, W. Huang, L. Wu, Z. Dong, Y. Zhang, B. Dong, X. Zhang, H. Zhang, *Small Methods* **2019,** *3,* 1900349.

[31] L. H. Zeng, M. Z. Wang, H. Hu, B. Nie, Y. Q. Yu, C. Y. Wu, L. Wang, J. G. Hu, C. Xie, F. X. Liang, L. B. Luo, *ACS Appl. Mater. Interfaces* **2013,** *5,* 9362.

[32] X. Zhang, J. Jiang, A. A. Suleiman, B. Jin, X. Hu, X. Zhou, T. Zhai, *Adv. Funct. Mater.* **2019,** *29,* 1906585.

[33] E. M. Vinod, A. K. Singh, R. Ganesan, K. S. Sangunni, *J. Alloys Compd.* **2012,** *537,* 127.

[34] H. Liu, S. Hussain, A. Ali, B. A. Naqvi, D. Vikraman, W. Jeong, W. Song, K.-S. An, J. Jung, *RSC Adv.* **2018,** *8,* 25514.

[35] C. M. Smyth, G. Zhou, A. T. Barton, R. M. Wallace, C. L. Hinkle, *Adv. Mater. Interfaces* **2021,** 2002050.

[36] F. Qin, Y. Hu, P. Hu, W. Feng, *Nanotechnology* **2020,** *31,* 115204.

[37] E. Y. Wang, L. Hsu, *J. Electrochem. Soc.* **1978,** *125,* 1328.

[38] Y. Tang, Z. Wang, P. Wang, F. Wu, Y. Wang, Y. Chen, H. Wang, M. Peng, C. Shan, Z. Zhu, S. Qin, W. Hu, *Small* **2019,** *15,* 1805545.

[39] N. V. Joshi, *Photoconductivity: Art, Science, and Technology,* Marcel Dekker, New York **1990**.

[40] H. Kind, H. Yan, B. Messer, M. Law, P. Yang, *Adv. Mater.* **2002,** *14,* 158.

[41] C. H. Liu, Y. C. Chang, T. B. Norris, Z. Zhong, *Nat. Nanotechnol.* **2014,** *9,* 273.

[42] F. H. Koppens, T. Mueller, P. Avouris, A. C. Ferrari, M. S. Vitiello, M. Polini, *Nat. Nanotechnol.* **2014,** *9,* 780.

[43] B. D. Boruah, A. Mukherjee, A. Misra, *Nanotechnology* **2016,** *27,* 095205.

[44] J. Luo, S. Li, H. Wu, Y. Zhou, Y. Li, J. Liu, J. Li, K. Li, F. Yi, G. Niu, J. Tang, *ACS Photonics* **2017,** *5,* 398.

Figures and their captions

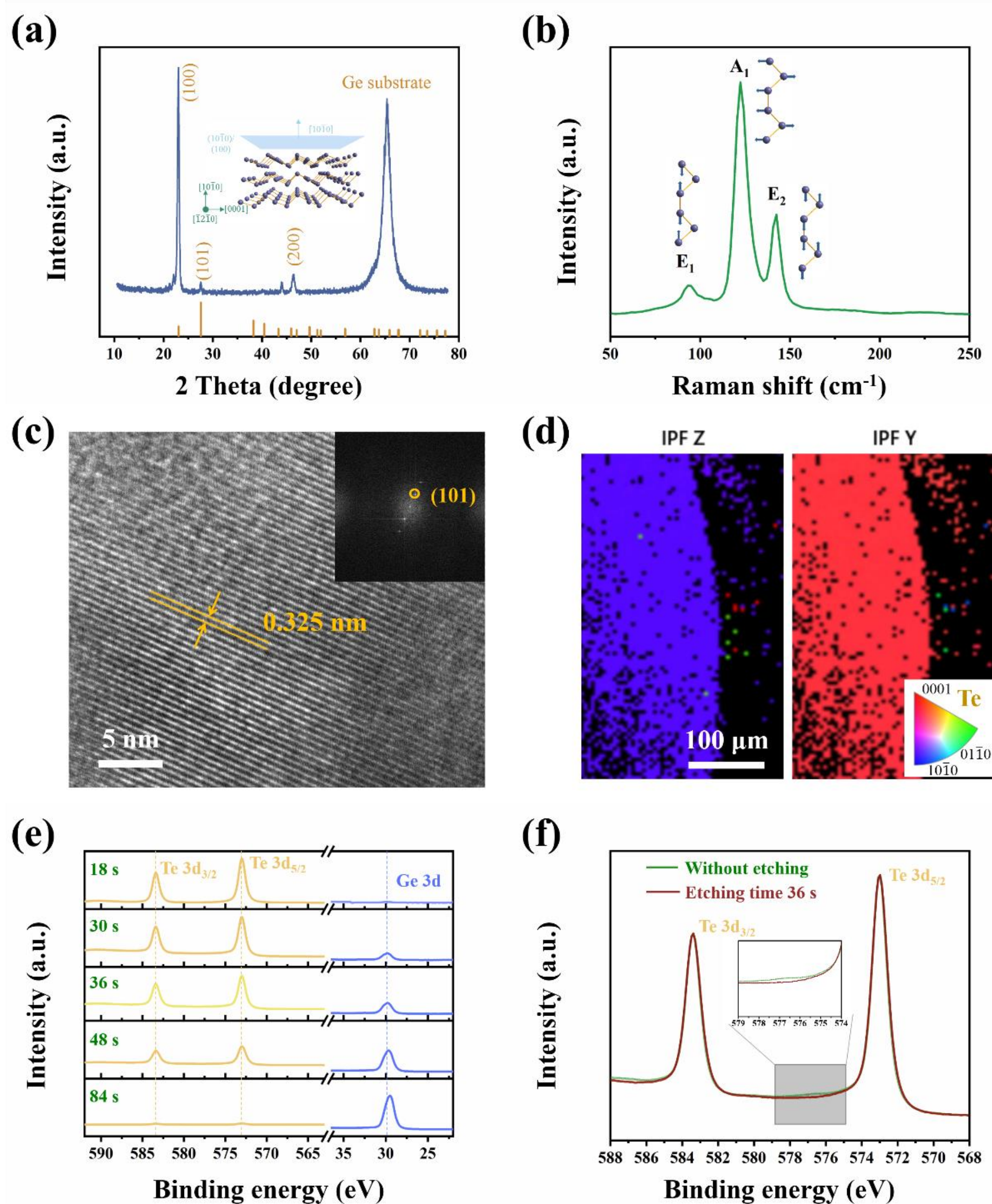

Figure 1. (a) XRD pattern of Te film and the inset shows 3D atomic structure diagram of hexagonal tellurium. (b) Raman spectrum of Te film. (c) TEM image of Te film. (d) Large-scale EBSD mapping on Te film. Left and right panels are inverse pore figures along *z*-axis (IPF-Z) and *y*-axis (IPF-Y), respectively, showing the highly $[10\bar{1}0]$-orientated crystallinity of as-grown Te film. (e) XPS depth profile of as-prepared Te/Ge heterojunction after consecutive ion etching steps for two different energy ranges near the Te 3d and Ge 3d peaks. Spectra are obtained for 5 different etching times of (top to bottom) t = 18, 30, 36, 48, and 84 s, respectively. (f) Residual Te peaks in Te film surface without etching and the interface intermixing regions with 36 s etching level. Inset plot reflecting the additional Te feature for Te-O bond.

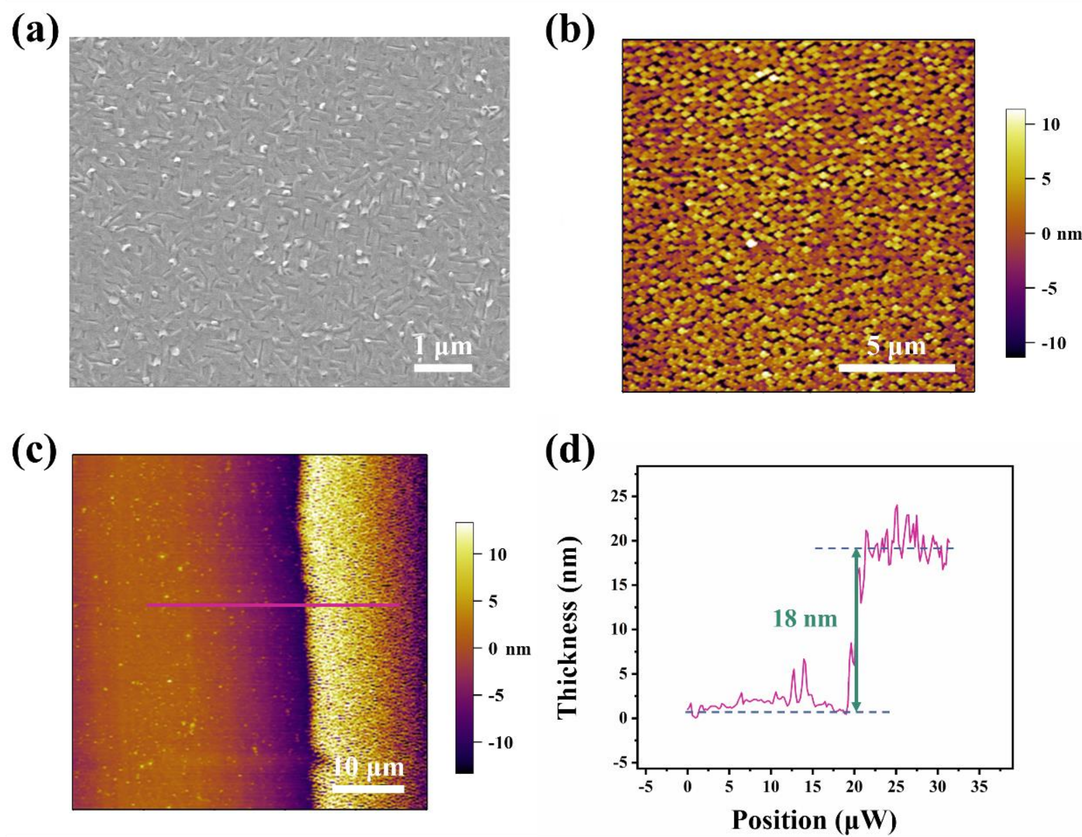

Figure 2. (a) SEM image of the Te film deposited on Ge substrate, scale bar is 1 μm. (b) AFM image of the Te film, scale bar is 5 μm. (c) AFM measurement cross the edge of Te film for illustrating thickness, scale bar is 10 μm. (d) The corresponding AFM height profile along the carmine line in (c).

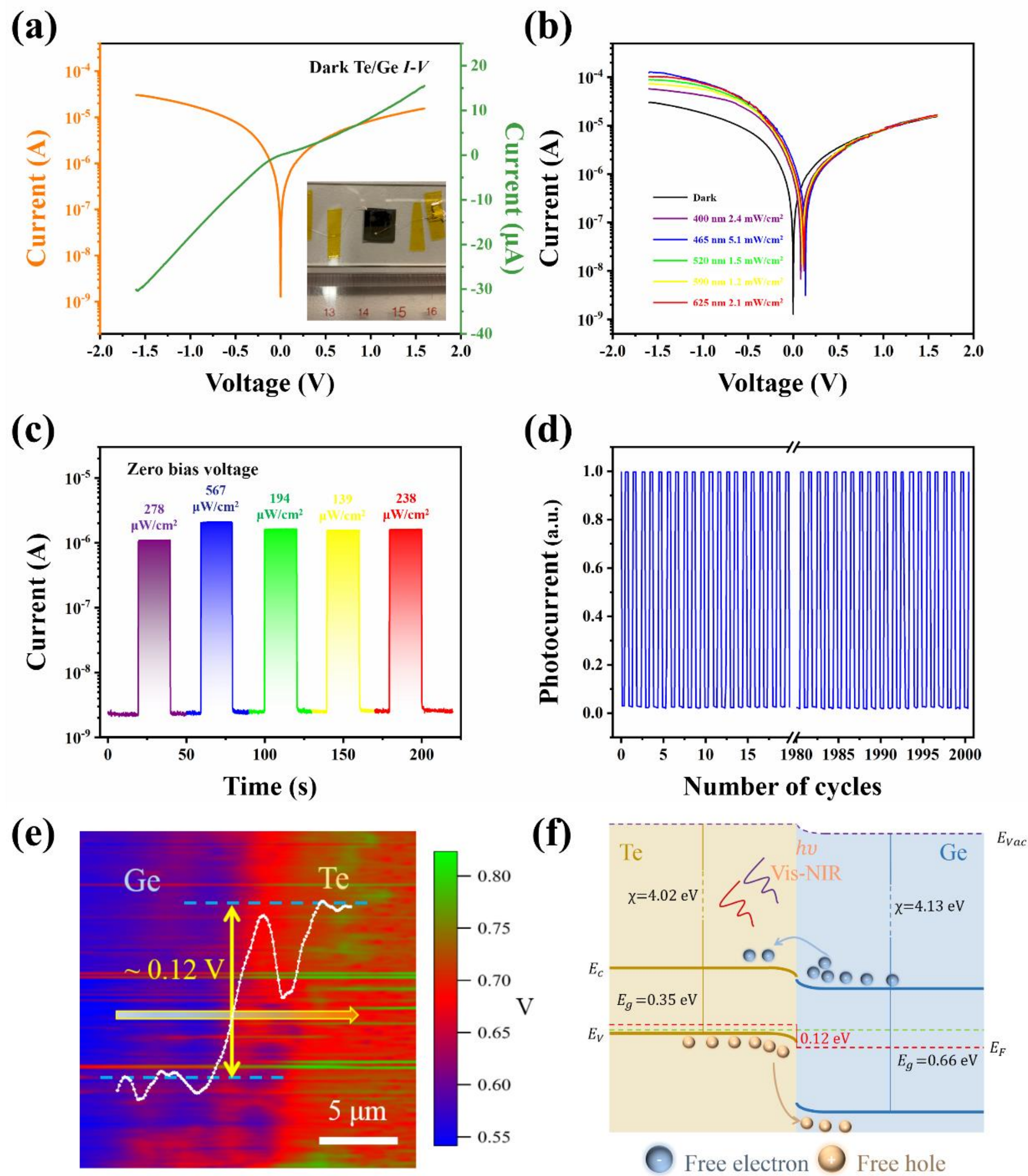

Figure 3. (a) *I*-*V* curves in dark of the Te/Ge heterojunction in linear and logarithmic coordinates, respectively. The inset shows an actual specimen photograph of Te/Ge heterostructure photodetector. (b) *I*-*V* curves of the Te/Ge heterojunction under visible light illumination with different wavelengths. (c) Time-resolved photoresponse properties under visible light illumination with different wavelengths. (d) The consecutive response measurement with 2000 continuous cycles. (e) KPFM surface potential map of an edge area in the Te/Ge heterojunction domain. The color contrast represents the surface potential distribution. Moreover, potential profile across the heterojunction region is presented in the illustration. (f) Schematic of energy band diagrams of the Te/Ge heterojunction under light illumination.

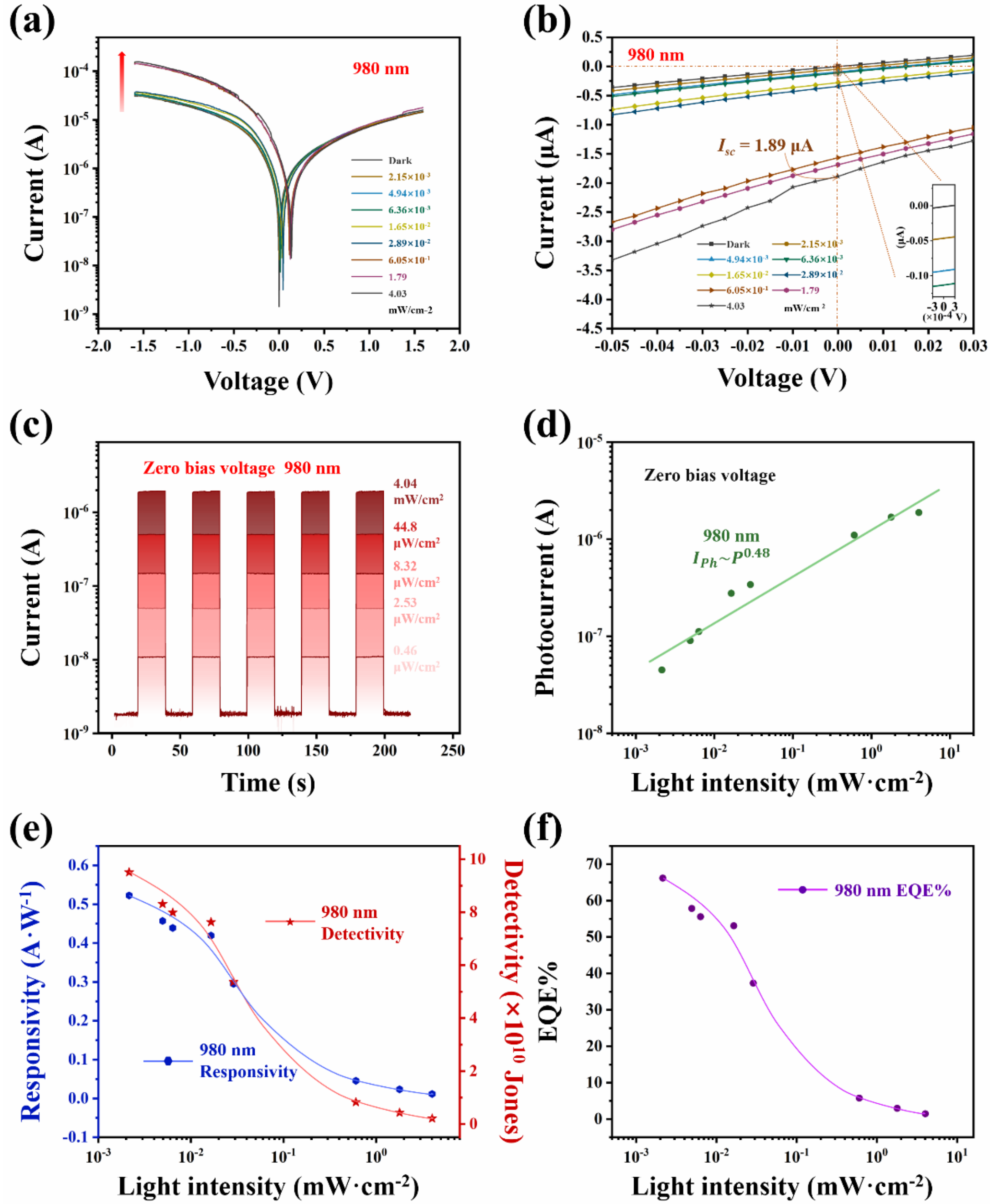

Figure 4. (a) *I-V* curves of the Te/Ge heterojunction photodetector measured under light illumination of 980 nm with varied light intensities. (b) Enlarged *I-V* curves showing the photovoltaic behavior of the Te/Ge heterojunction photodetector. (c) Time-resolved photoresponse of the Te/Ge heterojunction photodetector to different intensity lights of 980 nm. (d) Photocurrent as a function of the light intensity in double logarithmic coordinates for 980 nm light illumination. (e) Both responsivity and specific detectivity of the Te/Ge heterojunction photodetector with respect to the light intensity under 980 nm light illumination at zero bias voltage. (f) External quantum efficiency of the Te/Ge heterojunction photodetector.

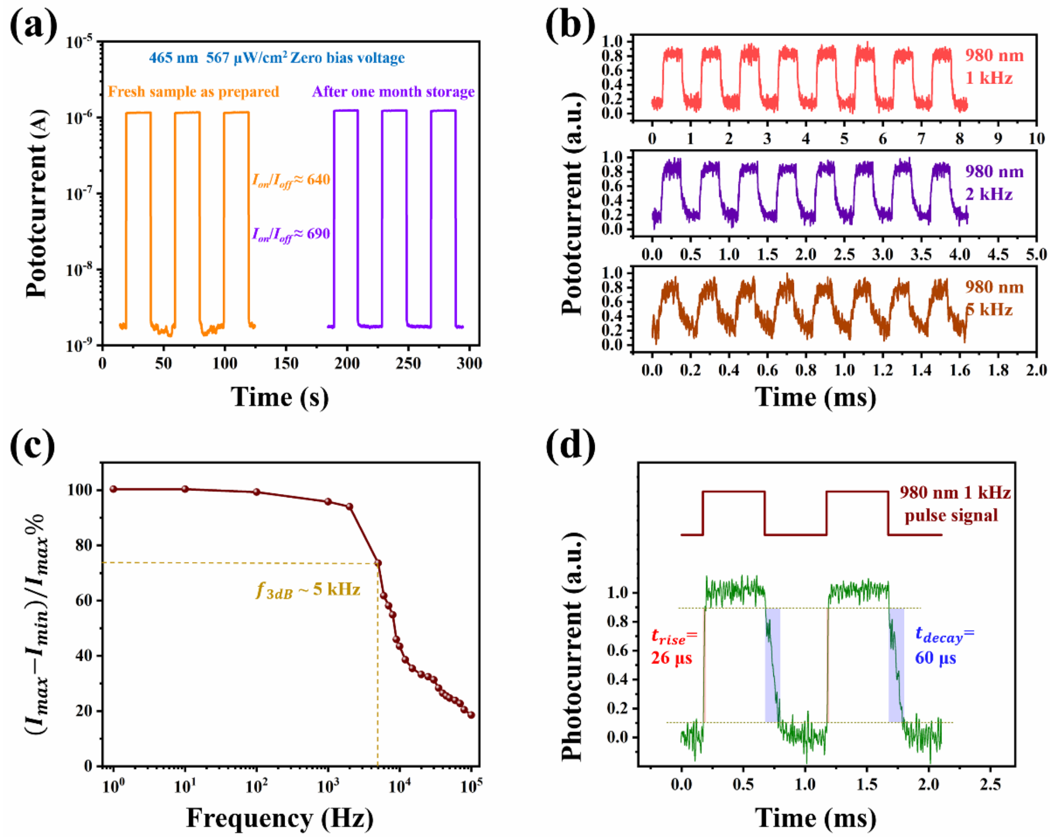

Figure 5. (a) Stability measurements by recording *I-T* curve of Te/Ge heterojunction photodetector for an as prepared sample and this one after one month storage in an air environment. (b) Photoresponse properties to pulsed light (980 nm) with frequencies of 1, 2, and 5 kHz, respectively. (c) Relative balance [$(I_{max}-I_{min})/I_{max}$] as a function of switching frequency. (d) Single normalized response for estimating the response speeds at 1 kHz.

Large-area Tellurium/Germanium Heterojunction was grwon using MBE method. Surface bonding activity of Ge alters the Te chain growth mode and induces the formation of large-area high crystalline-quality Te film. The virtue of interfacial built-in electric field is beneficial to facilitating the separation of photo-generated carriers. The photodetector is endowed with the self-powered nature and exhibits excellent optoelectronic performances.

Keywords: (tellurium, semiconductor germanium, heterojunction, large-area growth, self-powered photodetectors)

Beining Zheng, Zehan Wu, Feng Guo, Ran Ding, Jianfeng Mao, Maohai Xie, Shu Ping Lau, and Jianhua Hao**

Large-area Tellurium/Germanium Heterojunction Grown by Molecular Beam Epitaxy for High-performance Self-powered Photodetector

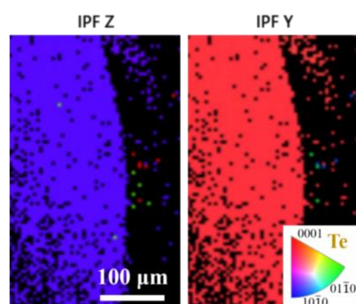

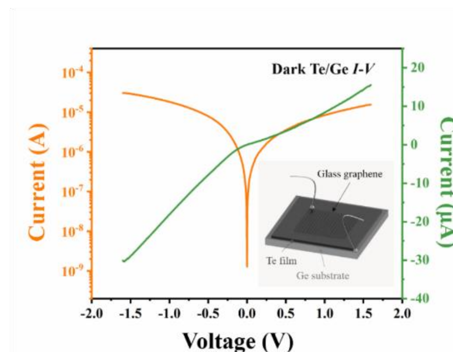

Copyright WILEY-VCH Verlag GmbH & Co. KGaA, 69469 Weinheim, Germany, 2016.

Supporting Information

Large-area Tellurium/Germanium Heterojunction Grown by Molecular Beam Epitaxy for High-performance Self-powered Photodetector

Beining Zheng, Zehan Wu, Feng Guo, Ran Ding, Jianfeng Mao, Maohai Xie, Shu Ping Lau, and Jianhua Hao**

Table S1. The performance comparison of some typical photodetector previously reported and the Te/Ge heterojunction in this work.

Materials (device setup)	Wavelength (nm)	Bias voltage (V)	Light intensity ($W\cdot m^{-2}$)	Photoresponsivity ($mA\cdot W^{-1}$)	Detectivity (Jones)	t_{rise} and t_{decay}	Ref.
2D Te nonosheets	Simulated light	0.6	530	126	2.4×10^{6}	50.4/70.2 ms	1
Te nanoplates	473	2	761.9	3.89×10^{5}	——	4.4/2.8 s	2
Quasi-2D Te nanoflakes, (optical cavity gating control)	~1400	5	——	1.3×10^{3}	2×10^{9}	0.4 ns	3
Te@Se roll to roll heterojunctions (electroly)	400	Applied	~10	1×10^{-1}	——	0.52/0.55 s	4
Te@Bi heterojunctions (electroly)	380	0.6	1.2×10^{3}	1.43×10^{-1}	5.14×10^{8}	0.09/ 0.09 s	5
Te nanomesh	365	Applied	~20	$\sim 2.4 \times 10^{-3}$	——	0.3/0.6 s	6
Si/ZnO	1064	0	0.48	4.3×10^{-1}	——	210/260 µs	7
$Ge/CH_3NH_3PbI_3$ perovskite heterostructure	1550	1	$\sim 1 \times 10^{-4}$	1.4	1×10^{8} (0.1 V)	2.1/5.7 ms	8
Graphene/Si heterojunction	488	Applied	2.6	0.435	7.69×10^{9}	1.2/3 ms	9
MoS_2/Si heterojunction	650	-2	——	1.19×10^{4}	2.1×10^{10}	30.5/71.6 µs	10
Te/Ge heterojunction	980	0	2.2×10^{-2}	522	9.50×10^{10}	14/105 µs	This work

Table S1 summarizes the key parameters of our Te/Ge heterojunction photodetector, compared to various Te-based photodetectors and some typical heterojunction photodetectors. The performance of our devices is comparable and even higher to that of the previously reported state-of-the-art Te-based devices. We need to point out that we mainly focus on the comparison of our Te/Ge heterojunction and Te-based photodetectors to show tremendous optoelectronic benefit from the junction

features. Various Te nanostructures also have great potential to achieve high responsivity, operational speed and other unique properties. [11, 12]

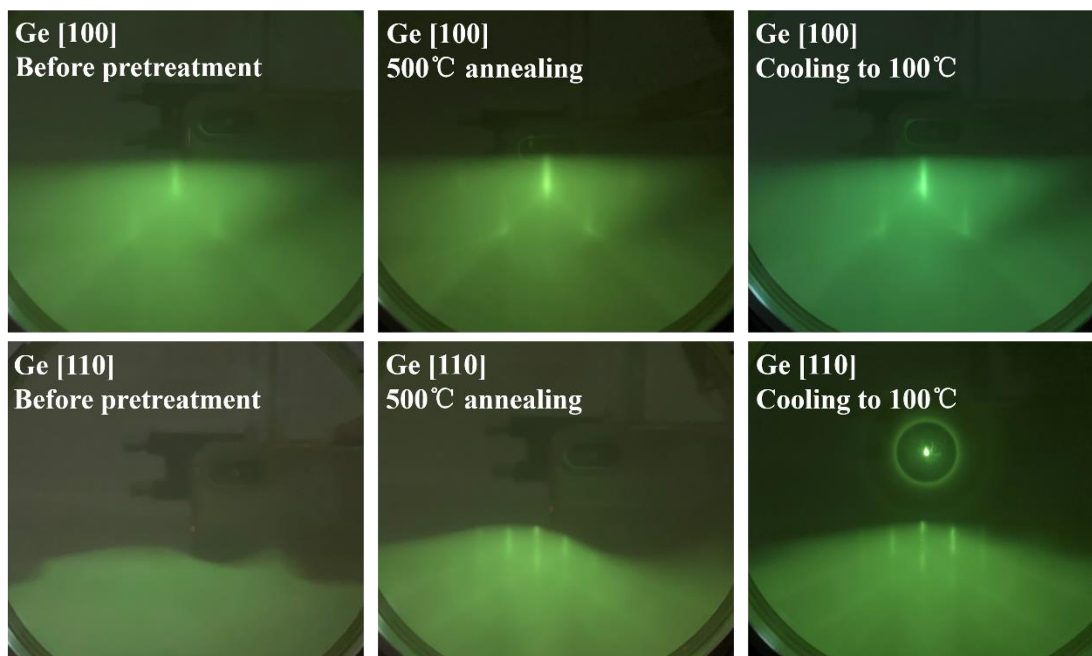

Figure S1. The revolution of RHEED pattern for Ge substrate pretreatment along the azimuths of Ge [100] and Ge [110].

As shown in Figure S1, the streak of reflection high-energy electron diffraction (RHEED) pattern became clear during substrate annealing treatment process. Especially, the evolution is obvious for Ge [110] azimuth. The clean Ge (001) substrate surface was observed by *in situ* RHEED. Along the azimuths Ge [110], the shadow of the holder fixture can be observed in the pattern images.

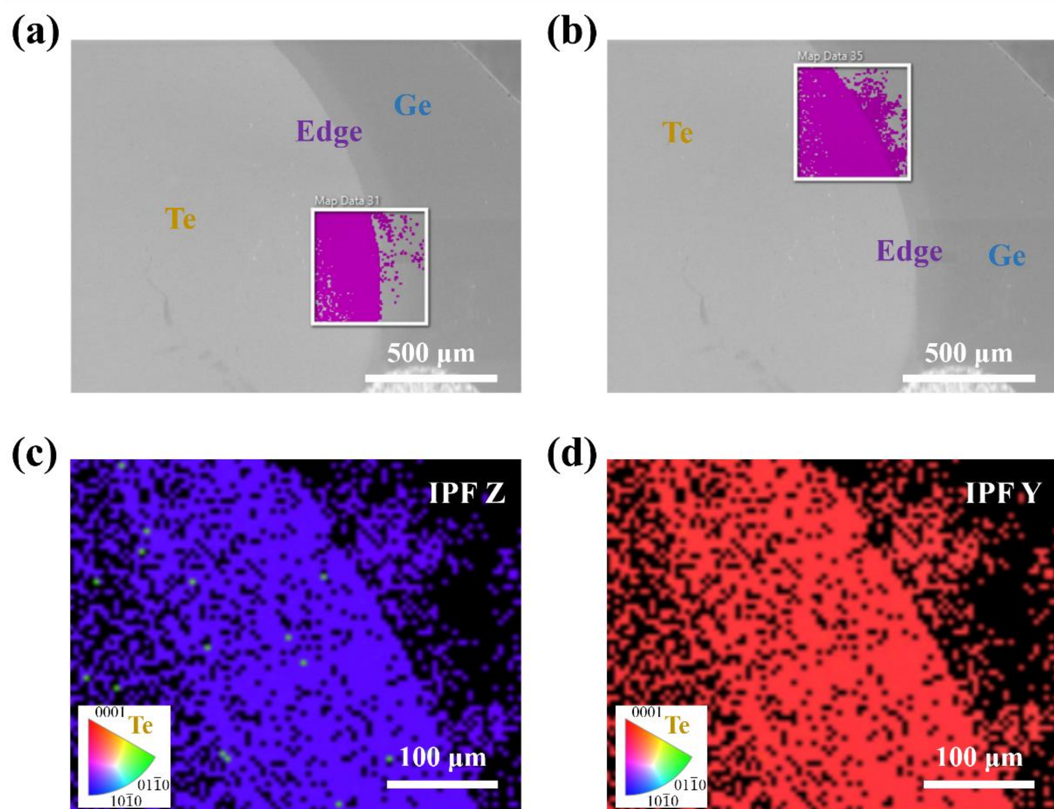

Figure S2. (a) Low magnification SEM image shows the mapping area for EBSD result in the main text. (b)-(d) Millimeter-scale EBSD mapping for another edge region of Te film, illustrating the highly homogeneous crystallinity of Te film.

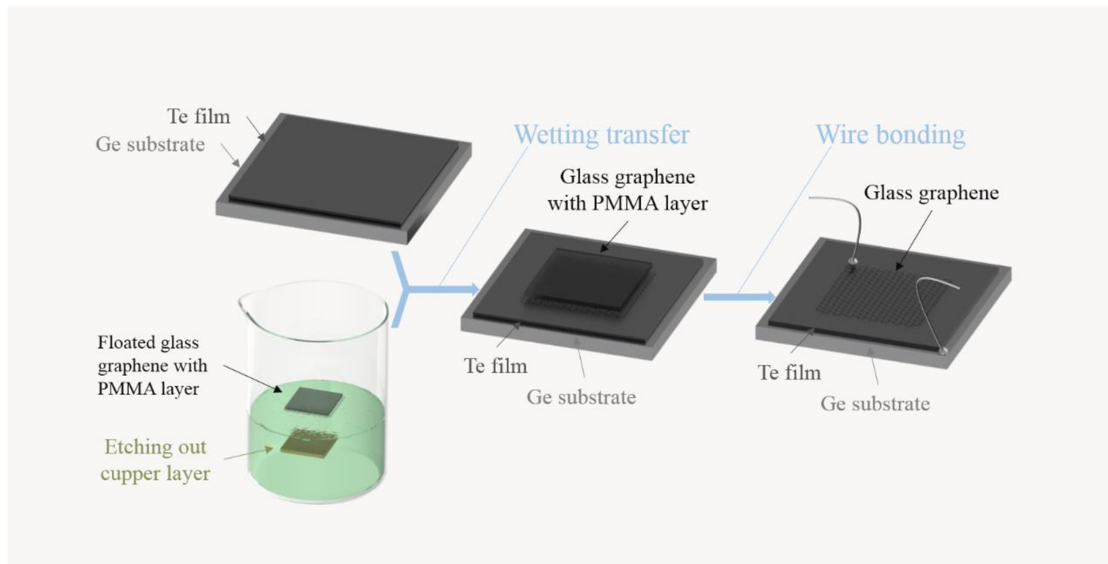

Figure S3. The sequential fabrication process and schematic diagram of the Te/Ge heterojunction photodetector.

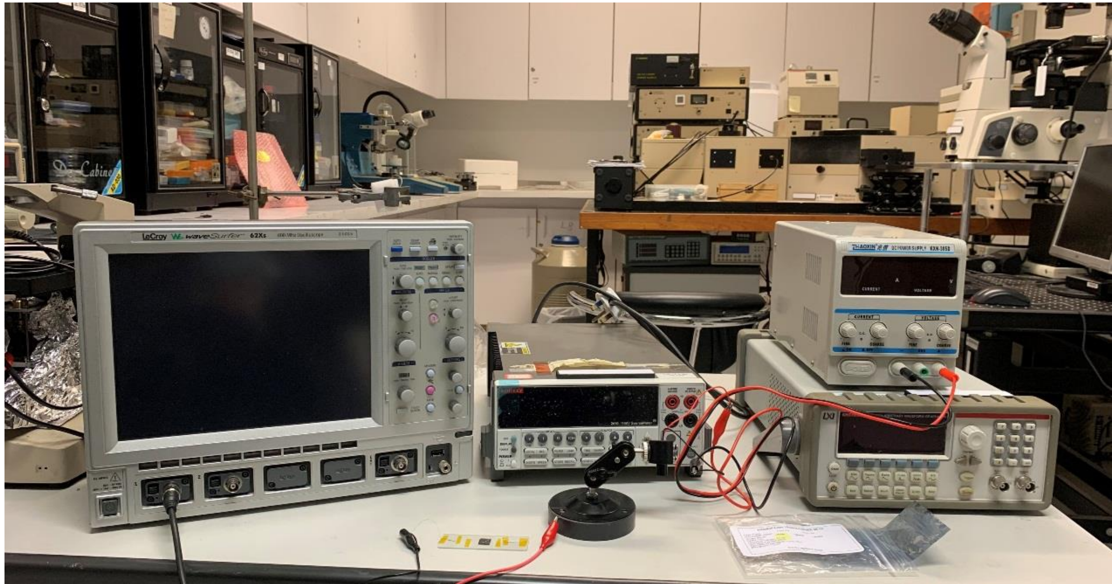

Figure S4. The actual photograph of optoelectronic measurement setup.

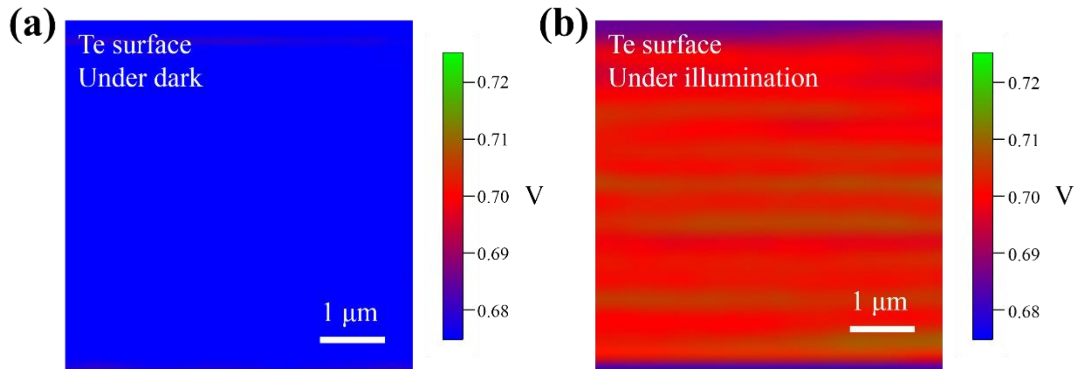

Figure S5. KPFM surface potential of Te layer under dark and illumination condition.

The influence of light source on the sample surface potential is showed in **Figure S5**. The color contrast of images presents the disparity of Te layer surface potential between the dark and illumination condition. Underdark condition, the sample surface potential was 700 mV relative to the KPFM tip. The value increased to 680 mV when the sample was under illumination. The observed shift in the surface potential possibly implies the carrier accumulation within the Te film with the injection of excitons. Under dark, the photogenerated carriers do not need to consider. Under illumination, there is a lot of photogenerated carriers. Because of depopulation of the energy states in the forbidden band gap, the photogenerated carriers quickly separated, and result in the change of surface potential Te. The result reflects the response of Te to light.

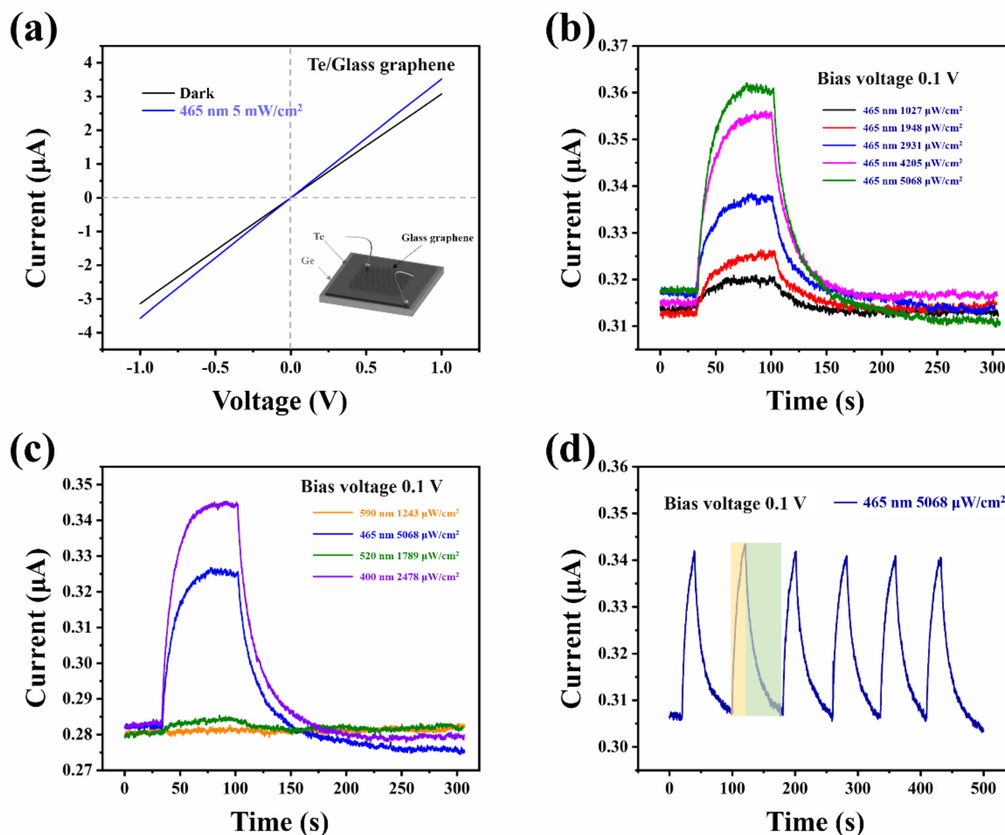

Figure S6. (a) The *I*-*V* curves of the structure based on g-graphene/Te film under dark and light illumination (5 mW·cm^{-2}, 450 nm blue light) condition. The diagram of the structure based on g-graphene/Te film. (b) Time-dependent photoresponse of g-graphene/Te film structure to on-off irradiation with different incident light intensity at a wavelength of 450 nm. The applied constant voltage is 0.1 V. (c) Time-dependent photoresponse of g-graphene/Te film structure to on-off irradiation under light illumination with different visible wavelengths. The applied constant voltage is 0.1 V. (d) Photoinduced current dynamics of g-graphene/Te film structure with constant voltage of 0.1 V.

The bilayer structure based on g-graphene/Te film was tested for checking the electrode performance of g-graphene and the photoconduction performance of intrinsic Te film. The g-graphene layer and Te film were wire-bonded after going through the same transfer processes, and the schematic diagram of the g-graphene/Te film structure is illustrated clearly in Figure S6. Figure S6(a) presents the *I*-*V* curves of the structure based on g-graphene/Te film under dark and light illumination (5 mW·cm^{-2}, 450 nm blue light) condition. Obviously, linear characteristic of *I*-*V* curves reveals that an

ohmic contact was formed between Te film and g-graphene. And charge carriers could experience barrierless transfer between Te film and g-graphene. The feasibility integrating graphene as electrode is fully demonstrated. In order to intuitively reflect the intrinsic Te photoconduction performance, time-dependent of photoresponse with different incident light intensity and with different visible wavelengths was performed at bias voltage of 0.1 V and pronounced photoconducting response was observed as shown in Figure S6(b) and (c). Photoinduced current dynamics of this structure illuminated by monochromatic blue are also recorded in the Figure S6(d). The applied constant voltage is 0.1 V and the time gap between on-off switching is 80 s. Despite the existence of external electric field enhancement, The low I_{on}/I_{off} ratio and the large rising and falling time of the photocurrent are demonstrated (under 465 nm, 5068 $\mu W \cdot cm^{-2}$ light illumination). This arises from the poor electron-hole pairs separating capacity of Te inherent structure.

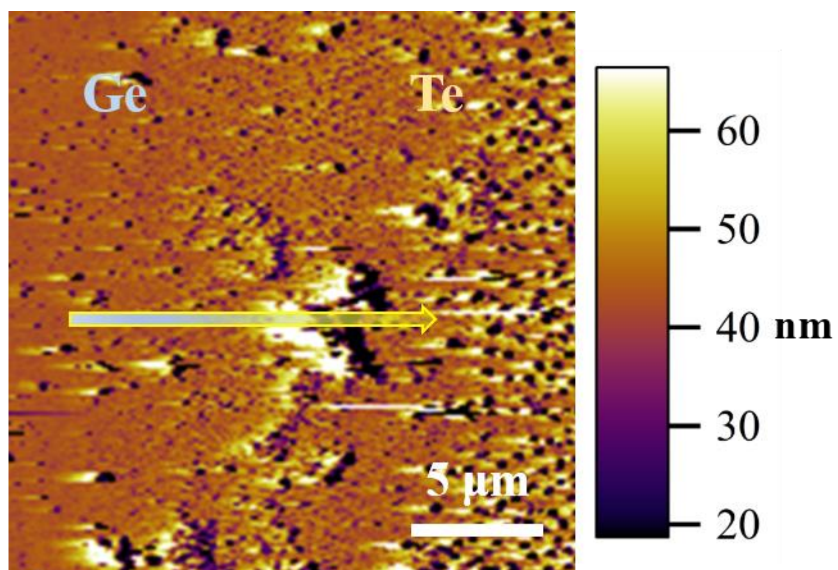

Figure S7. The AFM image corresponding to surface potential mapping area of the Te/Ge heterojunction.

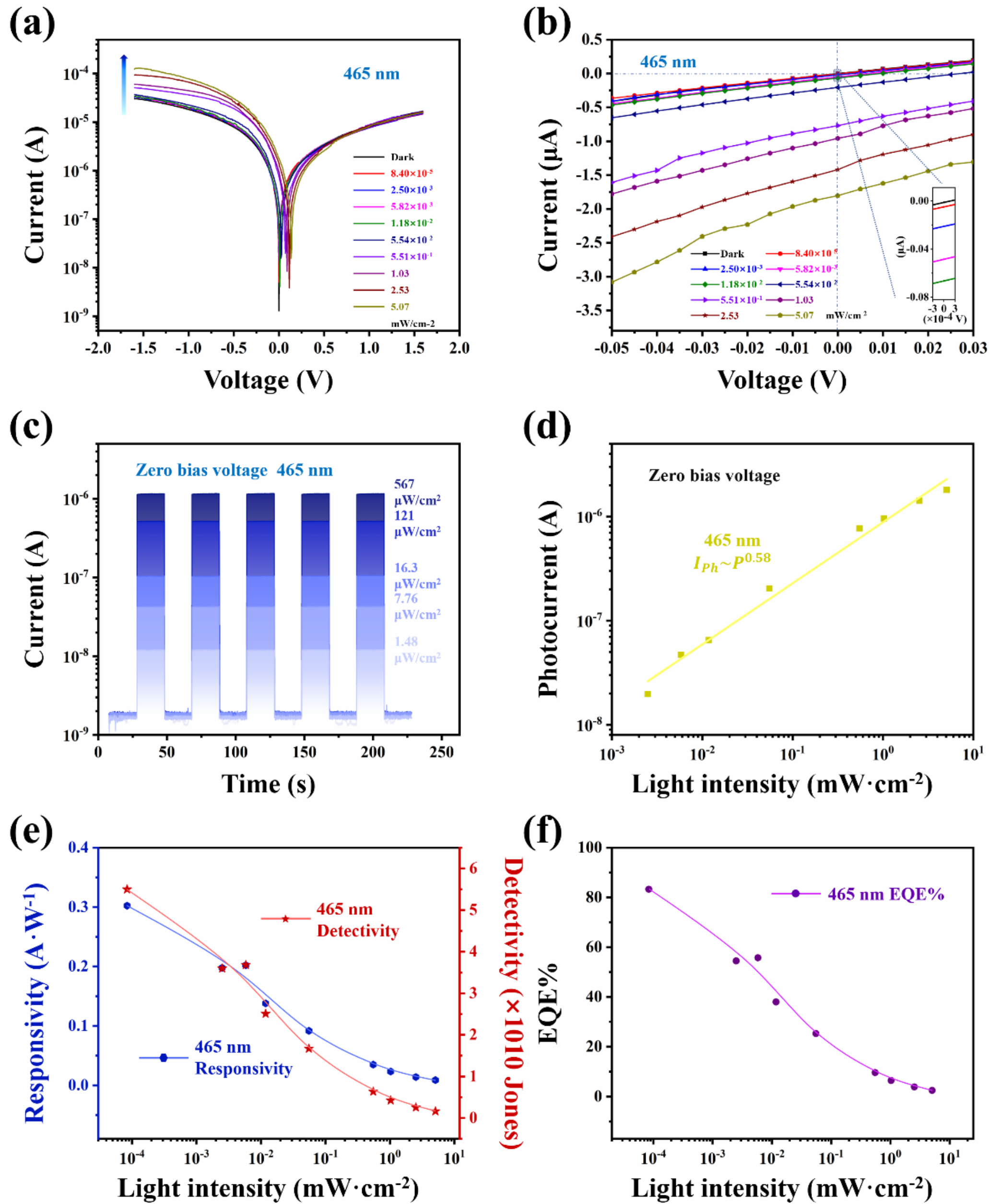

Figure S8. (a) *I-V* curves of the Te/Ge heterojunction photodetector measured under light illumination of 465 nm with varied light intensities. (b) Enlarged *I-V* curves measured under light illumination 465 nm with varied light intensities. (c) Time-resolved photoresponse of the Te/Ge heterojunction photodetector to different intensity lights of 465 nm. (d) Photocurrent as a function of the light intensity in double logarithmic coordinates for 465 nm light illumination. (e) Both responsivity and specific detectivity of the Te/Ge heterojunction photodetector with respect to the light intensity under 465 nm light illumination at zero bias voltage. (f) External quantum efficiency with respect to the light intensity under 980 nm light illumination at zero bias voltage.

As the key figure-of-merit parameters to evaluate the performance of a self-powered photodetector, responsivity (*R*), external quantum efficiency (*EQE*), and detectivity (*D**) of a photodetector can be calculated by the following equations: [13, 14]

$$R = \frac{I_{ph}}{P_{in}S} = \frac{I_{light} - I_{dark}}{P_{in}S}$$ **(Equation S1)**

$$EQE = \frac{I_{ph}/e}{P_{in}S/h\nu} = R\frac{hc}{e\lambda}$$ **(Equation S2)**

$$NEP = \frac{\overline{i_n^2}^{1/2}}{R}$$ **(Equation S3)**

$$D^* = \frac{(AB)^{1/2}}{NEP}$$ **(Equation S4)**

Where I_{light}, I_{dark}, P_{in} are the photocurrent, the dark current, light illumination intensity, repectively. *S* is the active illuminated area, *h* is Planck's constant, *c* is the light speed in a vacuum, *e* is the electron charge, and λ is the incident light wavelength, *A* is the effective area of the photodetector, *B* is the bandwidth, *NEP* is the noise equivalent power, $\overline{i_n^2}^{1/2}$ is the root mean square value of the noise current of the photodetector.

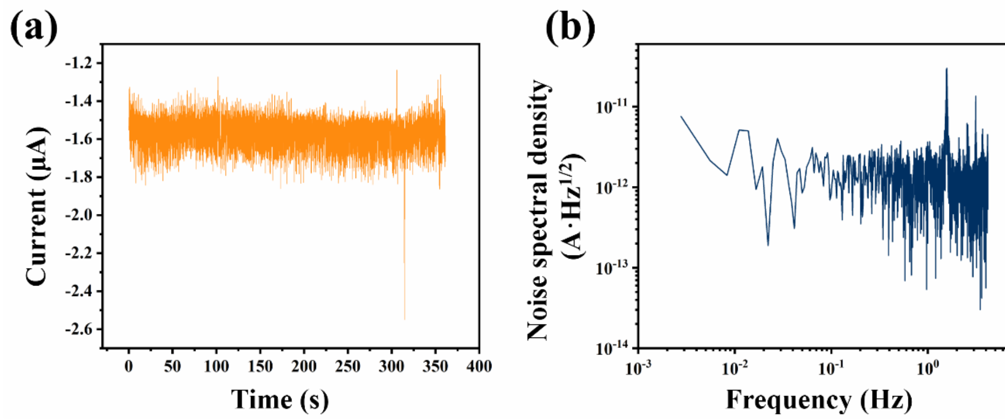

Figure S9. (a) The noise of the dark current of Te/Ge heterojunction photodetector at zero bias voltage. (b) Analysis of the Fourier transform of the dark current noise.

The noise level per unit bandwidth (1 Hz) of the photodetectors was measured to be ~ 1.1×10^{-12} A·Hz$^{-1/2}$.

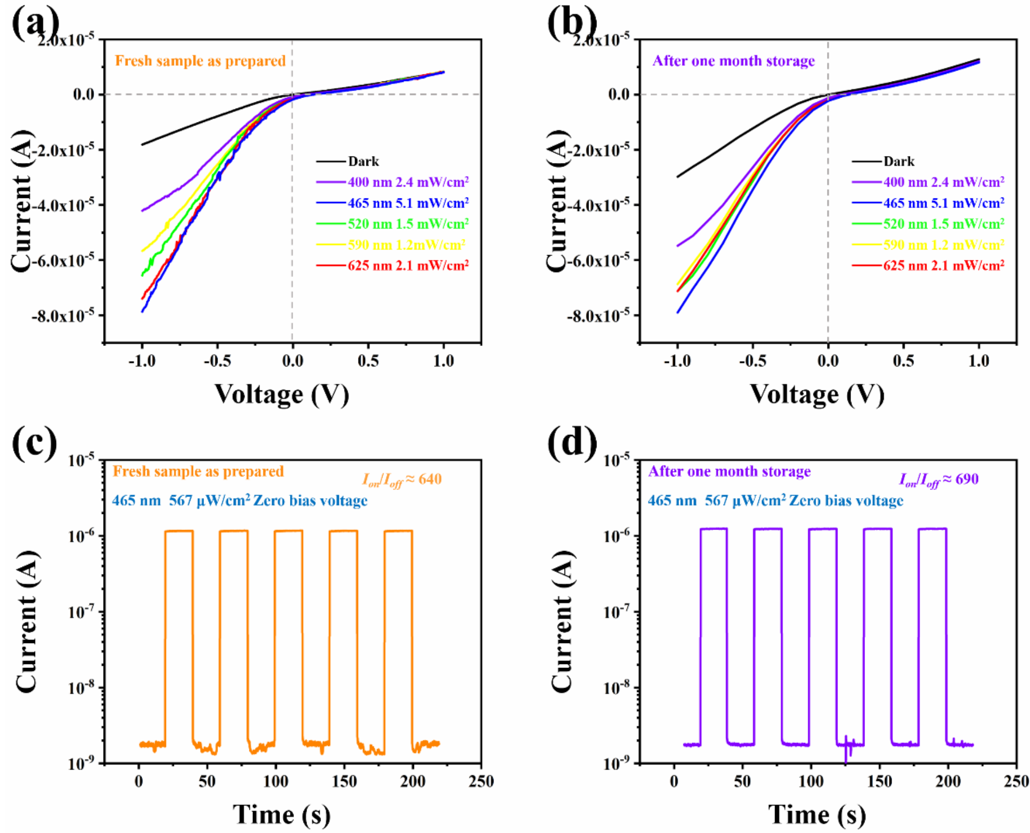

Figure S10. (a), (b) Stability measurements by recording *I-V* curve of Te/Ge heterojunction photodetector for an as prepared sample and this one after one month storage in an air environment. (c), (d) Stability measurements by recording *I-T* curve of Te/Ge heterojunction hotodetector for an as prepared sample and this one after one month storage in an air environment.

The Te/Ge heterojunction photodetector was stored in an air environment with the humidity of about 50%. The long-term stability of the unencapsulated device was compared by recording *I-V* and *I-T* curves. Figure S10(a) and (b) presents the *I-V* curves showing no decrement of photocurrent density with the initial curve. Meanwhile, the "on–off" responsing behavior of the device is given in Figure S10(c) and (d). It is noted that the I_{on}/I_{off} ratio as well as response speed is also not significantly affected. The as-prepared device exhibited much less performance degradation after a storage for over

30 days. It confirmed that the Te/Ge heterojunction photodetector has rather good stability for optical applications.

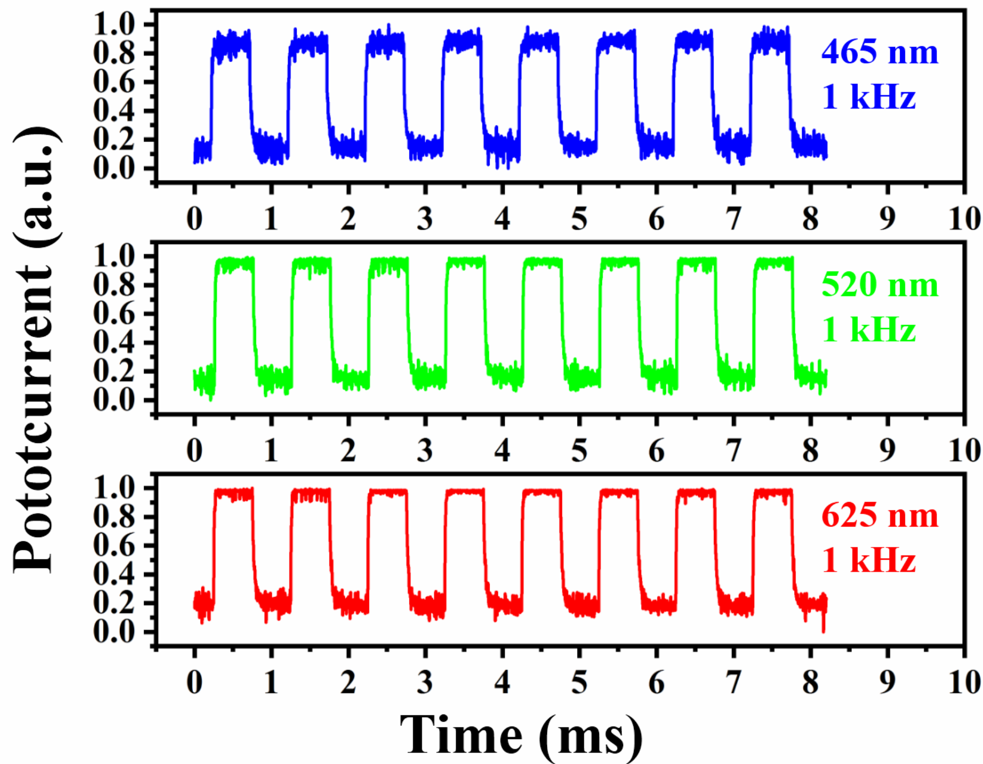

Figure S11. Time-dependent normalized photocurrent to 1 kHz frequency pulsed light signals with different visible radiation wavelengths of 465 nm, 520 nm, and 625 nm, respectively.

Visible wavelength LEDs driven by a function generator with 1 kHz frequency were used to produce pulsed light signals. Figure S11 depicts the time-dependent normalized photocurrent to pulsed light signals with different visible radiation wavelengths of 465 nm, 520 nm, and 625 nm, respectively. For the visible region, the Te/Ge heterostructure photodetector also exhibits expectant high-frequency photoresponse performance under 1 kHz signals illumination. Considering the limitations of these LEDs responsiveness, the response speeds to the pulsed laser of 980 nm with higher frequencies were further measured and elaborated in the main article.

References:

[1] Z. Xie, C. Xing, W. Huang, T. Fan, Z. Li, J. Zhao, Y. Xiang, Z. Guo, J. Li, Z. Yang, B. Dong, J. Qu, D. Fan, H. Zhang, *Adv. Funct. Mater.* **2018,** *28*, 1705833.

[2] Q. Wang, M. Safdar, K. Xu, M. Mirza, Z. Wang, J. He, *ACS Nano* **2014,** *8,* 7497.

[3] M. Amani, C. Tan, G. Zhang, C. Zhao, J. Bullock, X. Song, H. Kim, V. R. Shrestha, Y. Gao, K. B. Crozier, M. Scott, A. Javey, *ACS Nano* **2018,** *12,* 7253.

[4] W. Huang, Y. Zhang, Q. You, P. Huang, Y. Wang, Z. N. Huang, Y. Ge, L. Wu, Z. Dong, X. Dai, Y. Xiang, J. Li, X. Zhang, H. Zhang, *Small* **2019,** *15,* 1900902.

[5] Y. Zhang, F. Zhang, L. Wu, Y. Zhang, W. Huang, Y. Tang, L. Hu, P. Huang, X. Zhang, H. Zhang, *Small* **2019,** *15,* 1903233.

[6] S. Dang, S. D. Kang, T. Dai, X. Y. Ma, H. W. Li, W. Q. Zhou, G. L. Wang, P. Hu, Y. Sun, Z. H. He, F. M. Yu, X. Zhou, S. X. Wu, S. W. Li, *Nanotechnology* **2020,** *31,* 095502.

[7] X. Wang, Y. Dai, R. Liu, X. He, S. Li, Z. L. Wang, *ACS Nano* **2017,** *11,* 8339.

[8] W. Hu, H. Cong, W. Huang, Y. Huang, L. Chen, A. Pan, C. Xue, *Light Sci. Appl.* **2019,** *8,* 106.

[9] X. An, F. Liu, Y. J. Jung, S. Kar, *Nano Lett.* **2013,** *13,* 909.

[10] Y. Zhang, Y. Yu, L. Mi, H. Wang, Z. Zhu, Q. Wu, Y. Zhang, Y. Jiang, *Small* **2016,** *12,* 1062.

[11] Q. Xiao, X. Y. Li, Z. Q. Zhang, C. X. Hu, G. H. Dun, B. Sun, Y. Peng, Q. Wang, Z. Zheng, H. L. Zhang, *Adv. Electron. Mater.* **2020,** *6,* 2000240.

[12] X. Zhang, J. Jiang, A. A. Suleiman, B. Jin, X. Hu, X. Zhou, T. Zhai, *Adv. Funct. Mater.* **2019,** *29,* 1906585.

[13] M. S. Choi, D. Qu, D. Lee, X. Liu, K. Watanabe, T. Taniguchi, W. J. Yoo, *ACS Nano* **2014,** *8,* 9332.

[14] C. Xie, C. Mak, X. Tao, F. Yan, *Adv. Funct. Mater.* **2017,** *27,* 1603886.